Novel approach to characterize the deformation under Berkovich and spherical indentations: Study on magnesium single crystals

K. P. Raineesh [1], K. Sairam [2], K. Rajesh,[2] and K. Eswar Prasad [1,*]

[1]*Mechanics of Materials Group, Department of Metallurgy Engineering and Materials Science, IIT Indore, Simrol 453552, India*

[2]*Department of Materials Science and Metallurgical Engineering, IIT Hyderabad, Kandi 502285, India*

(Received 9 May 2021; revised 4 July 2021; accepted 23 July 2021; published 10 August 2021)

In this work, we have developed a mathematical framework to investigate the deformation response under Berkovich and spherical indenters. Nanoindentation experiments are carried out on two single-crystal magnesium (Mg) samples oriented for basal slip and tensile twinning. The indentation load vs penetration depth curves are then analyzed to explain the *pop-in* events with the help of Schmid factor analysis and to identify the favorable deformation modes directly beneath and around the indentation. These results explain why there is only a small difference in the values of hardness between the two orientations despite having a significant difference in their crystallographic orientations. In addition to this, the role of indenter tip radius on the formation of extension twins when indented along the crystallographic *c* axis is analyzed with the help of a simple analytical model.

DOI: 10.1103/PhysRevMaterials.5.083604

I. INTRODUCTION

Nanoindentation is by far the most popular technique to investigate the mechanical behavior of materials at small volumes due to its ability to apply indentation loads as small as a few nano-Newtons (nN) [1]. The indentation load P vs penetration depth h curves obtained from nanoindentation are extremely helpful in characterizing deformation events such as dislocation nucleation in crystalline materials [2–6], shear band nucleation and propagation in amorphous materials [7,8], phase transformations in crystals [9–11], and cracking events in brittle materials [12–14]. However, the analysis of plastic deformation during indentation, unlike uniaxial loading conditions, is not straightforward due to the multiaxial stress state present in the deformation zone under indentation. Though there have been a few studies in recent years to understand the onset of plastic flow under spherical indentation, no detailed mathematical framework is available for characterizing the plastic deformation under the widely used Berkovich indenter. In the current study, we developed a mathematical framework to understand the plastic deformation beneath the Berkovich indenter considering the indenter geometry, and the crystallographic orientation of the specimen. The analysis used in this study is generic to all crystalline materials although magnesium (Mg) is chosen for the current experiments. Unlike face centered and body centered cubic crystals, the plastic deformation in hexagonal close packed (hcp) Mg is highly anisotropic owing to the large differences in critical resolved shear stress (CRSS) for different slip and twin systems [15,16]. The slip systems include $\langle a\rangle$ slip on basal, prismatic, and pyramidal planes; $\langle c+a\rangle$ slip on pyramidal planes while twinning occurs on $\{10\bar{1}2\}\ \langle 10\bar{1}1\rangle$ and $\{10\bar{1}1\}\ \langle 10\bar{1}2\rangle$ systems, also referred to as extension and contraction twinning, respectively. Of all these, basal slip (BS) and extension twinning (ET) have the lowest CRSS and hence are ubiquitously seen during the plastic deformation in Mg. Under uniaxial loading conditions, the loading direction with respect to the crystal orientation determines the active deformation mode which differs significantly from one orientation to the other. However, during the indentation, BS and ET are observed to be the most commonly observed deformation modes for all the crystal orientations owing to their low CRSS and presence of multiaxial stress state [17–22] underneath the indenter. A few recent studies also reveal that indenter tip radius and penetration depth influence the formation of ET for loading along the crystallographic *c* axis. For the same penetration depths, Berkovich and Vickers indentations lead to profuse ET [19,20] while spherical indentation does not [21,22]. In the present work, we also explain this discrepancy with the help of a simple mathematical model in which the Schmid factor analysis for all the twin variants is performed by incorporating penetration depth and indenter radius.

II. MATERIALS AND EXPERIMENTS

Single-crystal Mg samples having 5N purity prepared using the Bridgman method are used for the indentation experiments. The orientations of the crystals, determined using electron backscattered diffraction (EBSD), are identified to be $[2\bar{1}\bar{1}2]$ and $[2\bar{1}\bar{1}0]$. For detailed EBSD analysis and images, the reader is referred to the work of Prasad *et al.* [23]. The Schmid analysis suggests that for uniaxial compression, the most favorable deformation modes for $[2\bar{1}\bar{1}2]$ and $[2\bar{1}\bar{1}0]$ are BS and ET, respectively [23]. The orientations $[2\bar{1}\bar{1}2]$ and $[2\bar{1}\bar{1}0]$ are hereafter referred to as *C*45 and *C*90, respectively, with the prefix representing the crystallographic *c* axis while the suffixes (45 and 90) represent the angle between the indentation direction and *c* axis [as shown in Fig. 1(a) with respect to the hcp unit cell]. Nanoindentation experiments are

*eswar@iiti.ac.in

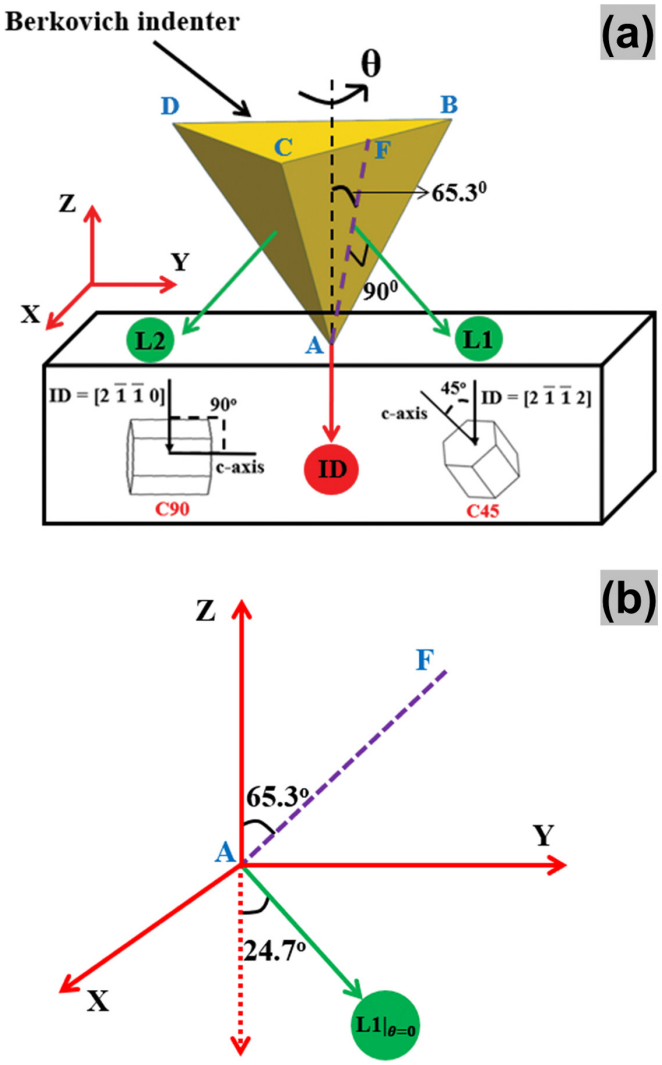

FIG. 1. (a) *ABC*, *ABD*, and *ACD* are three faces of the Berkovich indenter. *AF* is a line lying on *ABC*. **L1** and **L2** are normals to faces *ABC* and *ADC*, respectively. **ID** is the indentation direction along $[2\bar{1}\bar{1}0]$ in *C*90 and $[2\bar{1}\bar{1}2]$ in *C*45 samples. The indenter can be oriented at any arbitrary angle θ (rotation about the *Z* axis). For reference orientation, $\theta = 0$, indenter edge *BC* is along the *X* axis, the line *AF* and **L1** vector lie on the *ZY* plane as shown in (b).

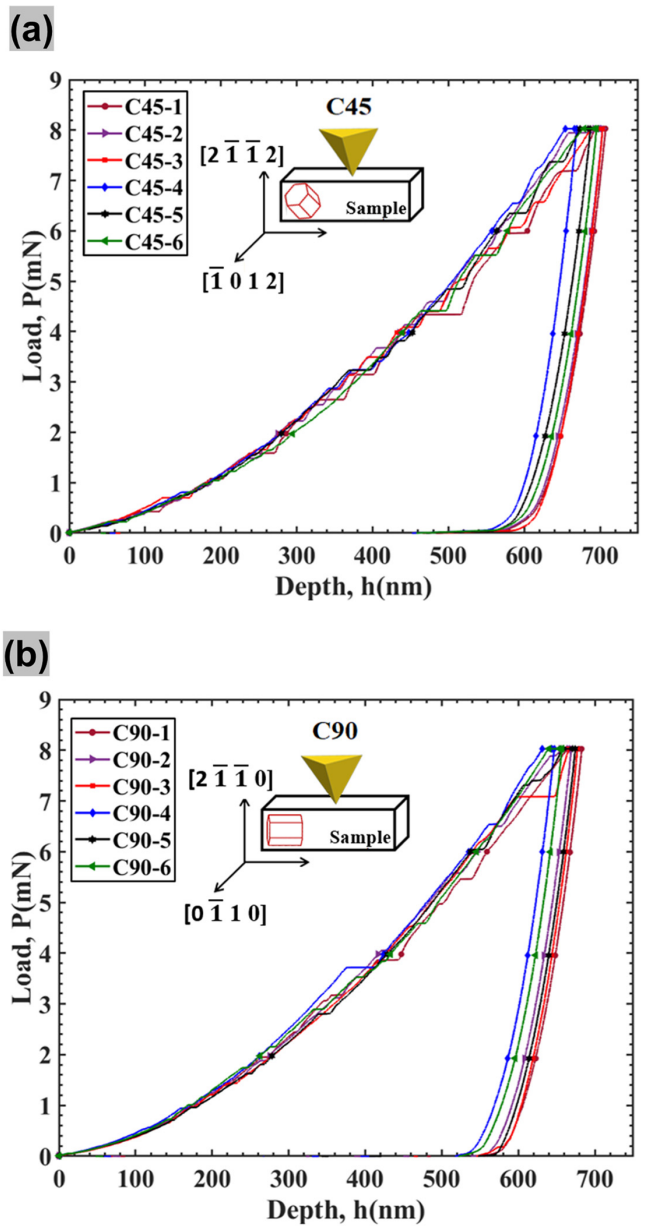

FIG. 2. Nanoindentation load *P* vs penetration depth *h* curves of (a) *C*45 and (b) *C*90 samples.

performed using a Berkovich indenter with a peak indentation load of 8 mN, with loading and unloading rates of 0.8 mN/s. The samples for nanoindentation are prepared by polishing the surfaces to be indented to a surface finish of 0.25 μm.

III. RESULTS AND DISCUSSIONS

Indentation load *P* vs penetration depth *h* curves obtained for *C*45 and *C*90 are shown in Figs. 2(a) and 2(b), respectively. It can be observed from Fig. 2 that all the loading curves exhibit discrete displacement bursts (also known as *pop-ins*) which are generally attributed to the dislocation/twin nucleation event in Mg. Previous experimental and molecular dynamics (MD) simulation studies of nanoindentation of Mg [20,21,24,25] clearly showed that the first pop-in in the loading curves corresponds to nucleation of dislocations. Prasad *et al.* [23] have shown that the stress drops during microcompression (equivalent to pop-in under constant strain rate loading) correspond to nucleation of deformation twins, so twinning is also expected to cause pop-in during nanoindentation as reported by Guo *et al.* [26]. Therefore, the first pop-in marks the onset of plasticity and the loading curves obey the Hertzian elastic contact equation until the first pop-in as shown in Fig. 3. The good agreement between the loading curves until the first pop-in (as shown in the inset of Fig. 3) is attributed to the high elastic isotropy of Mg.

It can be noticed from Fig. 2 that the penetration depth corresponding to maximum indentation load P_{max} is higher for *C*45 indicating that *C*45 is softer compared to *C*90. The hardness of the samples is computed using the Oliver-Pharr method [27,28] and the average hardness values *H* of *C*45 and

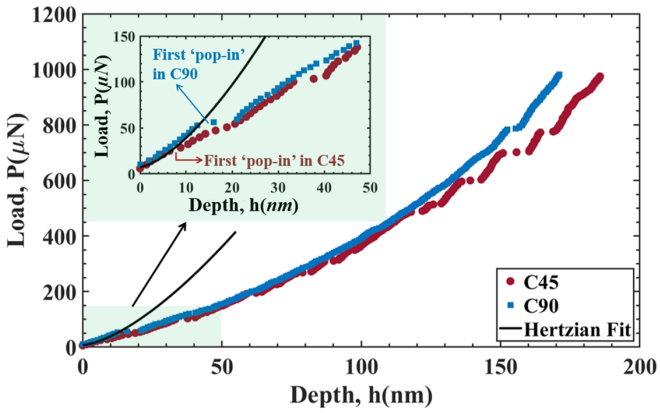

FIG. 3. Representative P vs h curves for $C45$ and $C90$ samples up to a load of 1 mN. The first pop-ins indicating the onset of plasticity are shown as a magnified view in the inset figure. Both curves are well described by the Hertzian elastic contact theory until the first pop-in.

$C90$ are found to be 539 ± 19 MPa and 586 ± 22 MPa, respectively, which differ only by 9%. Interestingly, Prasad *et al.* [23] performed uniaxial compression experiments and have reported the compressive flow stresses at 8% strain ($\sigma_{0.08}$) to be 60 and 372 MPa for $C45$ and $C90$, respectively, which differ by 520%, much higher than the difference observed in the case of H. The flow stress values are taken at 8% strain as it corresponds to the representative strain underneath a Berkovich indenter (stems of the geometry of the indenter) [29]. The significant difference in the flow stress between the two orientations under uniaxial compression is primarily due to the operation of contrasting deformation modes unlike indentation where multiple deformation modes are active because of the multiaxial stress state. However, there is no analytical solution to date to explain the reasons for small differences in H values as compared to the flow stress. In order to address this issue, we have developed a novel mathematical framework in this work by considering indenter geometry, the crystallographic orientation of the sample.

A. Mathematical model to characterize deformation under Berkovich indenter

The schematic of a Berkovich indenter is presented in Fig. 1(a) along with the important loading directions used in the analysis: **ID** represents the indentation direction, which is normal to the sample surface while **L1**, **L2**, and **L3** correspond to loading directions normal to the triangular faces of the indenter. Two such loading directions **L1** and **L2**, i.e., normals to the faces ABC and ADC of the indenter, are shown in Fig. 1(a). The model developed here is based on the Schmid factor analysis and does not consider the non-Schmid effects on the deformation. In magnesium, deformation by slip is mainly determined by the Schmid criterion and non-Schmid effects are negligible. Unlike slip, the mechanism of twinning in hcp metals is a debatable topic as it has been proposed that twin boundary motion is assisted by atomic shuffling [30–32] and movement of basal/prismatic or prismatic/basal interfaces contrary to the gliding of twinning dislocations [33–37]. However, in the current analysis, we have assumed that the ET occurs on the $\{10\bar{1}2\}\langle 10\bar{1}1\rangle$ twin system [38,39]. Beyerlein *et al.* [40] observed that, during the uniaxial compression of a Mg polycrystal, the twin variants with higher Schmid factor have a higher thickness assuming that the twin growth process obeys the Schmid criterion. However, in the same and other similar studies [41,42] it has been observed that twin variants with lower Schmid factor also nucleate, although their growth is restricted and accounts for a very small fraction of the total number of observed twins. It has been argued that these twins with negative or small Schmid factors were most likely introduced during the metallographic polishing of the section. Nevertheless, among the population of twins formed, a larger population is constituted by those with higher Schmid factor, indicating that twin nucleation also obeys the Schmid criterion.

Therefore, the Schmid factors, $m_{\mathbf{L1}}$, $m_{\mathbf{L2}}$, and $m_{\mathbf{L3}}$ (for BS and ET) corresponding to **L1**, **L2**, and **L3**, respectively, determine the prominent deformation mode around the indenter while Schmid factor $m_{\mathbf{ID}}$, corresponding to **ID**, indicates the favorable deformation mode directly beneath the indenter. In $C90$, **ID** is along $[2\bar{1}\bar{1}0]$ and $m_{\mathbf{ID}}$ for BS and ET is 0 and 0.38, respectively, and hence deformation is accommodated by ET directly beneath the indenter. In the case of $C45$, **ID** is along $[2\bar{1}\bar{1}2]$ and $m_{\mathbf{ID}}$ for BS is 0.49 which is the most favorable deformation mode directly beneath the indenter. Unlike $m_{\mathbf{ID}}$, the determination of $m_{\mathbf{L1}}$, $m_{\mathbf{L2}}$, and $m_{\mathbf{L3}}$ is not straightforward as they depend on the in-plane orientation of the indenter which is described by angle θ. If the indenter is oriented in such a way that the edge of the indenter, BC is along the X axis, then the line AF and **L1** lie in the ZY plane as schematically presented in Fig. 1(b). This orientation is taken as the $\theta = 0$ orientation and $\mathbf{L1}|_{\theta=0} = 0\hat{\boldsymbol{i}} + \sin(24.7)\hat{\boldsymbol{j}} - \cos(24.7)\hat{\boldsymbol{k}}$ where $\hat{\boldsymbol{i}}$, $\hat{\boldsymbol{j}}$, and $\hat{\boldsymbol{k}}$ represent the unit vectors along the X, Y, and Z directions, respectively, while the angle 24.7° arises due to the geometry of the Berkovich indenter. **L1** at any θ can be obtained by rotating $\mathbf{L1}|_{\theta=\mathbf{0}}$ by $\theta°$ about the Z axis.

$$\mathbf{L1} = R\begin{bmatrix} 0 \\ \sin(24.7) \\ -\cos(24.7) \end{bmatrix}, \tag{1}$$

$$R = \begin{pmatrix} \cos\theta & -\sin\theta & 0 \\ \sin\theta & \cos\theta & 0 \\ 0 & 0 & 1 \end{pmatrix}, \tag{2}$$

where R represents the rotation matrix about the Z axis in the counterclockwise direction. For any in-plane orientation θ, **L1** is expressed as $\mathbf{L1} = -\sin(\theta)\sin(24.7)\hat{\boldsymbol{i}} + \cos(\theta)\sin(24.7)\hat{\boldsymbol{j}} - \cos(24.7)\hat{\boldsymbol{k}}$. The Schmid factors for BS and ET systems in $C90$ corresponding to **L1** are calculated by the following procedure: Let α_p, β_p, and γ_p be the angles that the slip (or twin) plane normal makes with X, Y, and Z directions lying along [0001], $[01\bar{1}0]$, and $[2\bar{1}\bar{1}0]$, respectively, and let α_d, β_d, and γ_d be the angles that slip (or twin) direction makes with X, Y, and Z. Then for any slip or twin system $(hkil)$ $[uvtw]$, the above-mentioned angles can be found by crystallographic calculations [43]. The slip/twin plane normal $\boldsymbol{n_p}$ and slip/twin direction $\boldsymbol{d}$ are then represented by $\cos(\alpha_p)\hat{\boldsymbol{i}} + \cos(\beta_p)\hat{\boldsymbol{j}} + \cos(\gamma_p)\hat{\boldsymbol{k}}$ and $\cos(\alpha_d)\hat{\boldsymbol{i}} + \cos(\beta_d)\hat{\boldsymbol{j}} + \cos(\gamma_d)\hat{\boldsymbol{k}}$, respectively, in sample coordinate

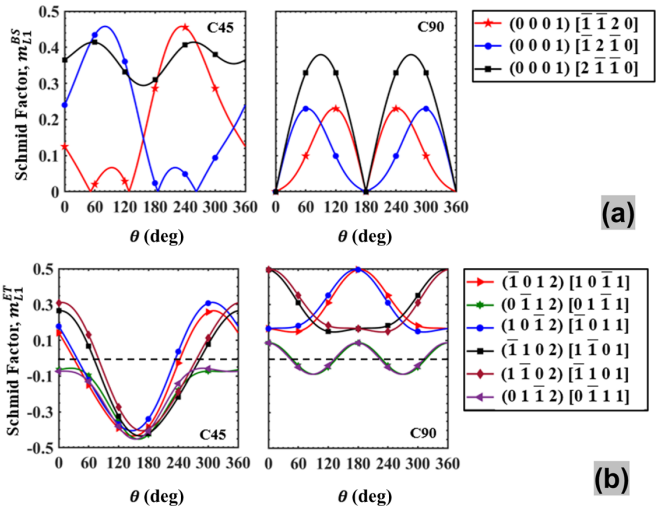

FIG. 4. The variation of m with θ for (a) basal slip and (b) extension twinning corresponding to loading along **L1**. The m corresponding to loading along **L2** and **L3** also can be read from the same plot based on the relation described in Eqs. (5) and (6).

system (X-Y-Z). The Schmid factor corresponding to **L1,** m_{L1} is given by $(\mathbf{L1}\cdot\boldsymbol{n_p})(\mathbf{L1}\cdot\boldsymbol{d})$ which is multiplied with a negative sign in the case of ET due to its polar nature while the sign is irrelevant for BS because of its nonpolar nature and hence absolute value is used for BS. Following this, m_{L1} for ET ($m_{\mathbf{L1}}^{\mathrm{ET}}$) and BS ($m_{\mathbf{L1}}^{\mathrm{BS}}$) are computed from Eqs. (3) and (4), respectively, as follows.

$$m_{\mathbf{L1}}^{\mathrm{ET}} = -\,[\mathbf{L1}\cdot\boldsymbol{n_p}]\cdot[\mathbf{L1}\cdot\boldsymbol{d}], \tag{3}$$

$$m_{\mathbf{L1}}^{\mathrm{BS}} = |[\mathbf{L1}\cdot\boldsymbol{n_p}]\cdot[\mathbf{L1}\cdot\boldsymbol{d}]|. \tag{4}$$

A similar procedure is employed to compute the Schmid factors for $C45$. The variation of $m_{\mathbf{L1}}^{\mathrm{BS}}$ and $m_{\mathbf{L1}}^{\mathrm{ET}}$ with θ is plotted for both the orientations as shown in Figs. 4(a) and 4(b), respectively. From the geometry of the Berkovich indenter, the directions **L1**, **L2**, and **L3** are 120° apart. Therefore, at any orientation of indenter, θ, the Schmid factors corresponding to **L2** and **L3** are related to **L1** by the Eqs. (5) and (6), respectively.

$$m_{\mathbf{L2}}|_{\theta} = m_{\mathbf{L1}}|_{\theta+240^{\circ}}, \tag{5}$$

$$m_{\mathbf{L3}}|_{\theta} = m_{\mathbf{L1}}|_{\theta+120^{\circ}}. \tag{6}$$

Therefore, the Schmid factors corresponding to **L2** and **L3** can also be obtained from the plot (Fig. 4) using Eqs. (5) and (6).

In the proposed model, the complex stress state underneath the indenter is resolved into compressive stress acting along the normal to the faces of the indenter. Brookes *et al.* [44] proposed a model (based on the Schmid factor analysis) in the early 1970s to analyze the hardness anisotropy. In the proposed model, the effective resolved shear stress ($\boldsymbol{\tau}^{\mathbf{e}}$) for all the possible slip systems around the indenter is computed considering that the tensile stress is being acted on the indenter face having a steeper slope. The active slip system is then predicted by comparing the $\boldsymbol{\tau}^{\mathbf{e}}$ vs θ curves with the H vs θ curve, where θ represents the in-plane orientation of the intender. However, one of the limitations of this analysis is that only one deformation mode is assumed to get activated underneath the indenter at a time. But in Mg, the literature studies [20–22,26,45,46] show the operation of both BS and ET simultaneously at different locations underneath the indenter. The advantage of the model presented in the current work is its capability to predict all the possible deformation modes (though we have presented only the most favorable modes, BS and ET) directly beneath and around the slanting faces of the indenter separately.

B. Active deformation modes underneath indenter in *C*90 and *C*45

It can be noticed from Fig. 4(a) that, for any θ, BS has a nonzero Schmid factor (at least one among $m_{\mathbf{L1}}$, $m_{\mathbf{L2}}$, and $m_{\mathbf{L3}}$) in both $C90$ and $C45$ and hence BS possibly occurs around the indenter in both orientations. Similarly, the Schmid factor for ET has non-negative values [at least one among $m_{\mathbf{L1}}$, $m_{\mathbf{L2}}$, and $m_{\mathbf{L3}}$ as shown in Fig. 4(b)] suggesting that the deformation by ET is also possible in both $C45$ and $C90$. Based on this, it can be interpreted that both ET and BS are active deformation modes in both orientations under Berkovich indentation which could be one of the reasons for similar hardness values for both orientations. Deformation by ET directly beneath and around the indenter [many twin variants have non-negative Schmid factor, Fig. 4(b)] can lead to a multicrystalline state in the subsurface deformation zone and hence irrespective of the initial orientation of the crystal, the material underneath the indenter behaves like a polycrystal whose volume increases with increase in indentation load. This is also a possible reason for similar hardness value for both orientations. Sánchez-Martín *et al.* [45] and Hiura *et al.* [47] also observed that the variation of H with crystal orientation is not very significant in Mg single crystals. At lower indentation loads, owing to their low CRSS, the BS gets activated more easily, while at high indentation loads, both ET and BS are feasible deformation mechanisms underneath the indentation [45]. Therefore, it is expected that the difference in hardness between the orientation is high at low indentation depths (due to the contrasting deformation mechanisms) and decreases with an increase in indentation depths. A detailed experimental study by varying the crystallographic orientation and indentation loads will provide further insights to understand the role of penetration depth on H.

Catoor *et al.* [21], and Somekawa *et al.* [24] have carried out nanoindentation experiments on the $C90$ orientation and showed (with the help of molecular static simulations and transmission electron microscope (TEM) imaging of the subsurface deformation zones) that the first pop-ins correspond to nucleation of basal dislocations. The Schmid factor analysis presented above suggests that BS is possible only around the indenter in $C90$ (due to "zero" Schmid factor directly beneath the indenter) while it is possible both directly beneath and around the indenter in $C45$. Therefore, the first pop-in in $C90$ and $C45$ is attributed to BS occurring around and beneath the indenter, respectively. One important observation from Fig. 3 is that the first pop-in load for BS is lower for $C45$ than $C90$.

This is due to the following reasons: (i) The Schmid factor for BS around the indenter in *C*90 [Fig. 4(a)] is lower than that for BS directly beneath the indenter in *C*45 (i.e., 49). (ii) At any given indentation load, the stress intensity is higher directly beneath the indenter than around it [48] and hence the CRSS for BS reaches a higher indentation load around the indenter. The first pop-in length is found to be higher for *C*90 than *C*45 which might be due to the higher elastic energy stored prior to the onset of plasticity. Zhang *et al.* [49] have argued that the elastic strain energy stored under the indenter (before the first pop-in) is proportional to the pop-in length and higher pop-in lengths are observed for orientations characterized by higher pop-in loads. Guo *et al.* [26] have observed a correlation between the onset of plasticity to the BS traces on the surface during the indentation of Mg single crystals along $[2\bar{1}\bar{1}0]$ (similar to *C*90 used in the current study) suggesting that the analysis used in the current study can capture the active deformation modes.

C. Mathematical model to characterize deformation under spherical indenter

Further, to understand the role of indenter radius and penetration depth on ET, a simple mathematic model is proposed for spherical indentation along the *c* axis. The planar section of the spherical indentation and important parameters used in the analysis are shown in Fig. 5(a). The green arrows represent the direction of indentation load and the hcp unit cell shown in the inset on the bottom left indicates the crystal orientation with respect to loading. The Schmid factor for ET, m^{ET}, increases with increasing the angle between the *c* axis and the compression axis which is normal to the indenter surface [43]. Therefore, m^{ET} is maximum corresponding to the load along the direction marked by $\mathbf{L}^{\mathbf{ET}}_{\mathbf{max1}} = 0\hat{\boldsymbol{i}} + \sin(\beta)\hat{\boldsymbol{j}} - \cos(\beta)\hat{\boldsymbol{k}}$, where β is the included angle between the loading direction and the *c* axis [as shown in Fig. 5(a)]. From the indenter geometry, $\cos\beta$ is expressed as $1-\frac{h}{r}$ where r and h are indenter radius and depth of penetration, respectively. Then $\mathbf{L}^{\mathbf{ET}}_{\mathbf{max1}}$ can be expressed in terms of the r and h as the following:

$$\mathbf{L}^{\mathbf{ET}}_{\mathbf{max1}} = 0\hat{\boldsymbol{i}} + \sqrt{1-\left(1-\frac{h}{r}\right)^2}\,\hat{\boldsymbol{j}} - \left(1-\frac{h}{r}\right)\hat{\boldsymbol{k}}. \tag{7}$$

Owing to the radial symmetry of the spherical indenter, all the lines (besides the $\mathbf{L}^{\mathbf{ET}}_{\mathbf{max1}}$) lying on the surface of the cone of semicone angle β make the same angle with the *c* axis. These directions ($\mathbf{L}^{\mathbf{ET}}_{\mathbf{max}}$) can be obtained by rotating $\mathbf{L}^{\mathbf{ET}}_{\mathbf{max1}}$ by ψ from 0° to 360° about the *Z* axis [as shown in Fig. 5(b)], where ψ is the in-plane rotation angle.

$$\mathbf{L}^{\mathbf{ET}}_{\mathbf{max}} = A\begin{bmatrix} 0 \\ \sqrt{1-\left(1-\frac{h}{r}\right)^2} \\ -\left(1-\frac{h}{r}\right) \end{bmatrix}, \tag{8}$$

where

$$A = \begin{bmatrix} \cos(\psi) & \sin(\psi) & 0 \\ -\sin(\psi) & \cos(\psi) & 0 \\ 0 & 0 & 1 \end{bmatrix}, \tag{9}$$

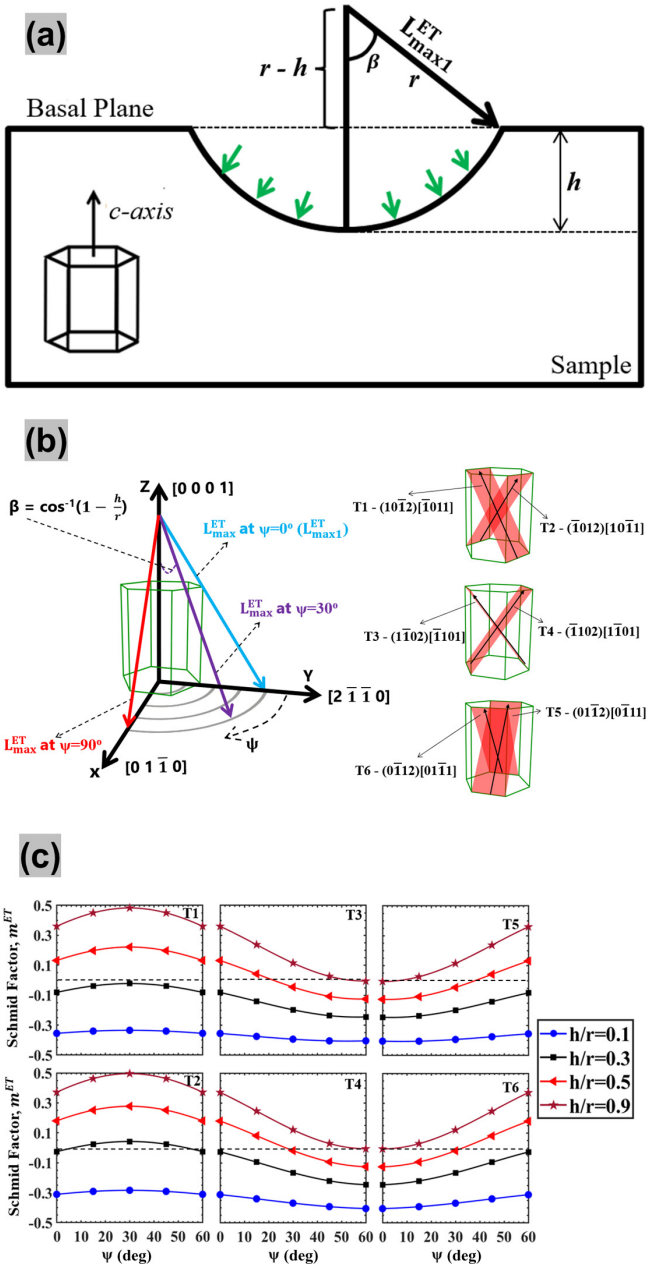

FIG. 5. (a) Schematic illustrating planar view of indentation along the *c* axis with spherical indenter of radius r. The m for ET increases with increasing angle between the *c* axis and loading direction. The maximum m for ET (m^{ET}) corresponds to loading along $\mathbf{L}^{\mathbf{ET}}_{\mathbf{max1}}(\psi = 0°)$ and all directions obtained by rotating $\mathbf{L}^{\mathbf{ET}}_{\mathbf{max1}}$ about the *Z* axis from $\psi = 0°$ to 360° as shown in (b). The variation of $m^{\mathrm{ET}}_{\mathrm{max}}$ with ψ for all six possible ET variants [shown in (b)] at different $\frac{h}{r}$ is plotted in (c). Owing to the symmetry of the hcp crystal, ψ up to only 60° is plotted.

is the rotation matrix about the *Z* axis in the clockwise direction.

The m^{ET} corresponding to the loading along $\mathbf{L}^{\mathbf{ET}}_{\mathbf{max}}$ is computed for all six possible ET variants [represented as T1–T6 along with their crystallographic planes and directions in Fig. 5(b)] and plotted as a function of ψ for different values of $\frac{h}{r}$ in Fig. 5(c). Both the $\mathbf{L}^{\mathbf{ET}}_{\mathbf{max}}$ and m^{ET} varies with ψ and $\frac{h}{r}$ and the variation of m^{ET} is plotted only until 60° in Fig. 5(c) as

it provides complete information (owing to the symmetry of the hcp crystal) for the other angles. For example, the m^{ET} for twin variant T2 at $\psi = 90^\circ$ is same as m^{ET} for twin variant T4 at $\psi = 30^\circ$ due to the crystallographic relation between them [Fig. 5(b)]. It can be noticed from Fig. 5(c) that at lower $\frac{h}{r}$ ratio, all twin variants have Schmid factor less than zero and hence ET is not a favorable deformation mode (ET is possible only if the Schmid factor is positive) and the possibility of ET increases with increase in $\frac{h}{r}$ ratio owing to the increase in m^{ET}. This is in agreement with the experimental observations of Sánchez-Martín *et al.* [45], Nayyeri *et al.* [50], and Zambaldi *et al.* [51] who observed ET at high $\frac{h}{r}$ ratio while it is absent at low $\frac{h}{r}$ ratio when the loading along the $\langle c \rangle$ axis. This is the reason why Shin *et al.* [19] and Gollapudi *et al.* [20] have observed ETs around the indenter for pyramidal indentation (having a small r and hence high $\frac{h}{r}$ ratio) contrary to Catoor *et al.* [21] and Kitahara *et al.* [22] who did not find ET around the indenter during spherica indentation with indenters having a higher r. Somekawa and Schuh [48] also observed a similar effect of r on nucleation of extension twins using finite element simulations. The current analysis clearly demonstrates that, during indentation along the c axis, ET is not possible directly underneath the indenter but its possibility to form around the edges of the indenter depends on the $\frac{h}{r}$ ratio. The locations of ET formed during indentation along the c axis carried out by Shin *et al.* [19] and Sánchez-Martín *et al.* [45] conform to our prediction. Further, as per the proposed analytical model, at sufficiently large penetration depths (or high indentation loads) both BS and ET are possible underneath the indentation irrespective of the crystallographic orientation and geometry of the indenter, so it is expected that the differences in H among different crystallographic orientations should be negligible at high indentation loads. In agreement with the above argument, the experimental results of Sánchez-Martín *et al.* [45] showed a little variation of hardness with crystallographic orientation at large penetration depths (∼2000 nm). However, a detailed experimental study needs to be performed to understand the variation of H on indentation load for Mg crystals having different crystallographic orientation.

IV. SUMMARY

In summary, a simple analytical model is proposed to predict the primary deformation modes under Berkovich and spherical indenters in single-crystal magnesium. The Schmid factors for basal slip and all the possible extension twin systems for Mg single crystals loaded along two crystallographic orientations (namely, $C45$ and $C90$) are determined considering the stress state around and under the indenter. Results show that basal slip is possible around the indenter even for crystals loaded along the a axis, despite having a low Schmid factor directly beneath the indenter indicating why hardness shows little dependence on crystal orientation in Mg. In the case of spherical indenters, the $\frac{h}{r}$ ratio markedly affects the deformation characteristics underneath the indenter and for indentation along the c axis, the possibility of twin formation depends on the $\frac{h}{r}$ ratio.

[1] C. A. Schuh, Nanoindentation studies of materials, Mater. Today **9**(5), 32 (2006).

[2] C. A. Schuh, J. K. Mason, and A. C. Lund, Quantitative insight into dislocation nucleation from high-temperature nanoindentation experiments, Nat. Mater. **4**, 617 (2005).

[3] D. Lorenz, A. Zeckzer, U. Hilpert, P. Grau, H. Johansen, and H. S. Leipner, Pop-in effect as homogeneous nucleation of dislocations during nanoindentation, Phys. Rev. B **67**, 172101 (2003).

[4] W. Wang, C. B. Jiang, and K. Lu, Deformation behavior of Ni_3Al single crystals during nanoindentation, Acta Mater. **51**, 6169 (2003).

[5] A. M. Minor, S. A. Syed Asif, Z. Shan, E. A. Stach, E. Cyrankowski, T. J. Wyrobek, and O. L. Warren, A new view of the onset of plasticity during the nanoindentation of aluminium, Nat. Mater. **5**, 697 (2006).

[6] O. Rodríguez de la Fuente, M. A. González, J. M. Rojo, J. A. Zimmerman, J. de la Figuera, J. C. Hamilton, and W. W. Pai, Dislocation Emission around Nanoindentations on a (001) fcc Metal Surface Studied by Scanning Tunneling Microscopy and Atomistic Simulations, Phys. Rev. Lett. **88**, 036101 (2002).

[7] C. A. Schuh and T. G. Nieh, A survey of instrumented indentation studies on metallic glasses, J. Mater. Res. **19**, 46 (2004).

[8] Y. I. Golovin, V. I. Ivolgin, V. A. Khonik, K. Kitagawa, and A. I. Tyurin, Serrated plastic flow during nanoindentation of a bulk metallic glass, Scr. Mater. **45**, 947 (2001).

[9] I. Zarudi, L. C. Zhang, and M. V. Swain, Behavior of monocrystalline silicon under cyclic microindentations with a spherical indenter, Appl. Phys. Lett. **82**, 1027 (2003).

[10] J. Jang, M. J. Lance, S. Wen, T. Y. Tsui, and G. M. Pharr, Indentation-induced phase transformations in silicon: Influences of load, rate and indenter angle on the transformation behavior, Acta Mater. **53**, 1759 (2005).

[11] J. Jang, M. J. Lance, S. Wen, and G. M. Pharr, Evidence for nanoindentation-induced phase transformations in germanium, Appl. Phys. Lett. **86**, 131907 (2005).

[12] D. S. Harding, W. C. Oliver, and G. M. Pharr, Cracking during nanoindentation and its use in the measurement of fracture toughness, Mater. Res. Soc. Symp. Proc. **356**, 663 (1995).

[13] K. E. Prasad and K. T. Ramesh, Hardness and mechanical anisotropy of hexagonal SiC single crystal polytypes, J. Alloys Compd. **770**, 158 (2019).

[14] A. B. Mei, H. Kindlund, E. Broitman, L. Hultman, I. Petrov, J. E.Greene, and D. G. Sangiovanni, Adaptive hard and tough mechanical response in single-crystal B1 VN_x ceramics via control of anion vacancies, Acta Mater. **192**, 78 (2020).

[15] J. Zhang and S. P. Joshi, Phenomenological crystal plasticity modeling and detailed micromechanical investigations of pure magnesium, J. Mech. Phys. Solids **60**, 945 (2012).

[16] W. B. Hutchinson and M. R. Barnett, Effective values of critical resolved shear stress for slip in polycrystalline magnesium and other hcp metals, Scr. Mater. **63**, 737 (2010).

[17] E. C. Burke and W. R. Hibbard, Plastic deformation of magnesium single crystals, JOM **4**, 295 (1952).

[18] H. Yoshinaga and R. Horiuchi, On the nonbasal slip in magnesium crystals, Trans. Jpn. Inst. Met. **5**, 14 (1964).

[19] J. H. Shin, S. H. Kim, T. K. Ha, K. H. Oh, I. S. Choi, and H. N. Han, Nanoindentation study for deformation twinning of magnesium single crystal, Scr. Mater. **68**, 483 (2013).

[20] S. Gollapudi, M. A. Azeem, A. Tewari, and U. Ramamurty, Orientation dependence of the indentation impression morphology in a Mg Alloy, Scr. Mater. **64**, 189 (2011).

[21] D. Catoor, Y. F. Gao, J. Geng, M. J. N. V. Prasad, E. G. Herbert, K. S. Kumar, G. M. Pharr, and E. P. George, Incipient plasticity and deformation mechanisms in single-crystal Mg during spherical nanoindentation, Acta Mater. **61**, 2953 (2013).

[22] H. Kitahara, T. Mayama, K. Okumura, Y. Tadano, M. Tsushida, and S. Ando, Anisotropic deformation induced by spherical indentation of pure Mg single crystals, Acta Mater. **78**, 290 (2014).

[23] K. E. Prasad, K. Rajesh, and U. Ramamurty, Micropillar and macropillar compression responses of magnesium single crystals oriented for single slip or extension twinning, Acta Mater. **65**, 316 (2014).

[24] H. Somekawa, T. Tsuru, A. Singh, S. Miura, and C. A. Schuh, Effect of crystal orientation on incipient plasticity during nanoindentation of magnesium, Acta Mater. **139**, 21 (2017).

[25] B. Selvarajou, J. H. Shin, T. K. Ha, I. S. Choi, S. P. Joshi, and H. N. Han, Orientation-dependent indentation response of magnesium single crystals: Modeling and experiments, Acta Mater. **81**, 358 (2014).

[26] T. Guo, F. Siska, and M. R. Barnett, Distinguishing between slip and twinning events during nanoindentation of magnesium alloy AZ31, Scr. Mater. **110**, 10 (2016).

[27] W. C. Oliver and G. M. Pharr, Measurement of hardness and elastic modulus by instrumented indentation: Advances in understanding and refinements to methodology, J. Mater. Res. **19**, 3 (2004).

[28] W. C. Oliver and G. M. Pharr, An improved technique for determining hardness and elastic modulus using load and displacement sensing indentation experiments, J. Mater. Res. **7**, 1564 (1992).

[29] *Nanoindentation Testing BT—Introduction to Contact Mechanics*, edited by A. C. Fischer-Cripps (Springer New York, New York, 2000), pp. 7, 25.

[30] J. Wang, S. K. Yadav, J. P. Hirth, C. N. Tomé, and I. J. Beyerlein, Pure-shuffle nucleation of deformation twins in hexagonal-close-packed metals, Mater. Res. Lett. **1**, 126 (2013).

[31] B. Y. Liu, J. Wang, B. Li, L. Lu, X. Y. Zhang, Z. W. Shan, J. Li, C. L. Jia, J. Sun, and E. Ma, Twinning-like lattice reorientation without a crystallographic twinning plane, Nat. Commun. **5**, 3297 (2014).

[32] B. Li and E. Ma, Atomic Shuffling Dominated Mechanism for Deformation Twinning in Magnesium, Phys. Rev. Lett. **103**, 035503 (2009).

[33] A. Serra, D. J. Bacon, and R. C. Pond, The crystallography and core structure of twinning dislocations in H.C.P. metals, Acta Metall. **36**, 3183 (1988).

[34] A. Serra and D. J. Bacon, Computer simulation of twinning dislocation in magnesium using a many-body potential, Philos. Mag. A **63**, 1001 (1991).

[35] J. Wang, J. P. Hirth, and C. N. Tomé, $(\bar{1}012)$ Twinning nucleation mechanisms in hexagonal-close-packed crystals, Acta Mater. **57**, 5521 (2009).

[36] K. E. Prasad and K. T. Ramesh, In-situ observations and quantification of twin boundary mobility in polycrystalline magnesium, Mater. Sci. Eng. A **617**, 121 (2014).

[37] B. Y. Liu, L. Wan, J. Wang, E. Ma, and Z. W. Shan, Terrace-like morphology of the boundary created through basal-prismatic transformation in magnesium, Scr. Mater. **100**, 86 (2015).

[38] B.-Y. Liu, K. E. Prasad, N. Yang, F. Liu, and Z.-W. Shan, *In-situ* quantitative tem investigation on the dynamic evolution of individual twin boundary in magnesium under cyclic loading, Acta Mater. **179**, 414 (2019).

[39] V. Kannan, K. Hazeli, and K. T. Ramesh, The mechanics of dynamic twinning in single crystal magnesium, J. Mech. Phys. Solids **120**, 154 (2018).

[40] I. J. Beyerlein, L. Capolungo, P. E. Marshall, R. J. McCabe, and C. N. Tome, Statistical analyses of deformation twinning in magnesium, Philos. Mag. **90**, 2161 (2010).

[41] J. Wang, I. J. Beyerlein, and C. N. Tomé, An atomic and probabilistic perspective on twin nucleation in Mg, Scr. Mater. **63**, 741 (2010).

[42] C. N. Tomé, I. J. Beyerlein, J. Wang, and R. J. McCabe, A multiscale statistical study of twinning in magnesium, JOM **63**, 19 (2011).

[43] X. L. Nan, H. Y. Wang, L. Zhang, J. B. Li, and Q. C. Jiang, Calculation of Schmid factors in magnesium: Analysis of deformation behaviors, Scr. Mater. **67**, 443 (2012).

[44] C. A. Brookes, J. B. O. Neill, and B. A. W. Redfern, Anisotropy in the hardness of single crystals, Proc. R. Soc. London, Ser. A **322**, 73 (1971).

[45] R. Sánchez-Martín, M. T. Pérez-Prado, J. Segurado, and J. M. Molina-Aldareguia, Effect of indentation size on the nucleation and propagation of tensile twinning in pure magnesium, Acta Mater. **93**, 114 (2015).

[46] T. Guo, F. Siska, J. Cheng, and M. Barnett, Initiation of basal slip and tensile twinning in magnesium alloys during nanoindentation, J. Alloys Compd. **731**, 620 (2018).

[47] F. Hiura, R. K. Mishra, M. Lukitsch, and M. Niewczas, Nanoindentation studies of twinned magnesium single crystals, in *Magnesium Technology 2012*, edited by S. N. Mathaudhu, W. H. Sillekens, N. R. Neelameggham, and N. Hort (Wiley, New York, 2012), p. 117.

[48] H. Somekawa and C. A. Schuh, Effect of crystal orientation on nanoindentation behavior in magnesium, Metall. Mater. Trans. A **47**, 3227 (2016).

[49] G. P. Zhang, W. Wang, B. Zhang, J. Tan, and C. S. Liu, On rate-dependent serrated flow behavior in amorphous metals during nanoindentation, Scr. Mater. **52**, 1147 (2005).

[50] G. Nayyeri, W. J. Poole, C. W. Sinclair, and S. Zaefferer, The role of indenter radius on spherical indentation of high purity magnesium loaded nearly parallel to the *c*-axis, Scr. Mater. **137**, 119 (2017).

[51] C. Zambaldi, C. Zehnder, and D. Raabe, Orientation dependent deformation by slip and twinning in magnesium during single crystal indentation, Acta Mater. **91**, 267 (2015).